

Interfacial stress assessment at the cracked zones in CFRP retrofitted RC beams

Ata Hojatkashani^{1a} and Mohammad Zaman Kabir^{*2}

¹University of Applied Science and Technology, Tehran, Iran

²Civil Engineering Department, Amirkabir University of Technology (Tehran Polytechnic), Tehran, Iran

(Received August 1, 2011, Revised September 13, 2012, Accepted November 1, 2012)

Abstract. In this work, an experimental examination was carried out to study interfacial stresses developed at the junction zones between carbon fiber reinforced plastic (CFRP) fabrics (~1 mm thickness) and tensile concrete portion in CFRP retrofitted RC beams. In this respect, initially six similar RC beams of 150 × 150 × 1000 mm dimensions were prepared. Three of which were strengthened with CFRP fabrics at the tensile side of the beams. Furthermore, a notch was cut at the center of the bottom surface for all of the studied beams. The notch was 15 mm deep and ran across the full width of tension side of the beams. The mentioned interfacial stresses could be calculated from strains measured using strain gauges mounted on the interface zone of the tensile concrete and the CFRP sheet. Based on the results obtained, it is shown that interfacial stresses developed between CFRP fabrics and RC beam had a noticeable effect on debonding failure mode of the latter. The load carrying capacity of CFRP strengthened RC specimens increased ~75% compared to that of the control RC beams. This was attributed to the enhancement of flexural mode of the former. Finally, finite element analysis was also utilized to verify the measured experimental results.

Keywords: experimental examination; CFRP strengthened RC beam; interfacial stress; critical zones; debonding failure mode; finite element analysis

1. Introduction

Recently, the use of composite materials for strengthening of concrete structures has become a common practice in structural rehabilitation industry. In this respect, externally bonded fiber reinforced plastic (FRP) fabrics has been considered as an interesting candidate for repairing and retrofitting of RC beams due to their high strength to weight ratio, easy installation and cost effectiveness (Meier 1997). CFRP sheets have been extensively used to strengthen RC beams both in field and laboratory (Labossiere *et al.* 2000). Duthinh *et al.* (2004) examined RC beams and after the cracking of the beams subjected to service loading, strengthened them with CFRP sheets and tested them under four point flexural bending eventually, resulted in the effective increase of the flexural strength.

*Corresponding author, Associate Professor, E-mail: mzkabir@aut.ac.ir

^aAssistant Professor, E-mail: hojatkashani@gmail.com

However, these suffer from debonding and peeling at some critical zones. Various authors (Jones *et al.* 1980, Van Gemert 1980, Oehlers *et al.* 1990) based on flexural test measurements carried out on steel-to-concrete and composite-to-concrete joints, have confirmed that plate separation occurred due to high local interfacial bond stresses and peeling forces at the end of plates.

For the flexural FRP strengthened RC beams, it is important to prevent the premature interface failure modes such as debonding. This mode of failure is due to crack propagation in adhesive layer which resulted from stress transfer between the concrete and the bonded FRP soffit plate. In fact, the distributed stresses adjacent to the junction zones of the FRP-concrete interface were found to depend on the tensile strength of concrete (Triantafillou *et al.* 1992), the concrete surface preparation (Zibara *et al.* 1995), and thickness and strength of the adhesive (Quantrill *et al.* 1996). However, considering the high tensile strength of most utilized adhesives, effect of the latter can be ignored. Debonding damage generally occurs in the concrete adjacent to the adhesive-to-concrete interface and is referred to as intermediate flexural crack-induced interfacial debonding or intermediate flexural shear crack-induced interfacial debonding (Teng *et al.* 2002). Hence, debonding may initiate at a flexural or a mixed flexural shear crack away from the plate ends and then propagates towards one of the plate ends. The interfacial failure mode can be also due to the crack propagation in the concrete parallel to the bonded plate and adjacent to the adhesive-to-concrete interface (Teng *et al.* 2002) leading to local concrete failure. To achieve a better understanding of the developed shear stresses distributions at the cracked zones and peeling off normal stress at the plate end in FRP retrofitted RC beams, others (Lau *et al.* 2001, Leung 2001, Smith *et al.* 2001, Hu *et al.* 2004, Goloti *et al.* 2004, Teng *et al.* 2005, Zou *et al.* 2007, Kabir *et al.* 2008, Huang *et al.* 2011) proposed theoretical and numerical models. For instance, considering stress distribution in the adhesive layer, researchers proposed differential equations in order to estimate peeling off and shear stresses at the plate end (Teng *et al.* 2005). In addition, in a study carried out by Leung (2001) interfacial stress τ was related to the longitudinal stress σ_p in the plate, as well as longitudinal displacement at the plate u_p and at the bottom of the beam u_b through the following

$$\tau = t d\sigma_p/dx = G(u_p - u_b)/h \quad (1)$$

where t = plate thickness; h = adhesive thickness; and G = adhesive shear modulus.

Furthermore, in another study using strain compatibility assumption a closed form exponential equation for the shear stress distribution in the adhesive layer at the cracked region was presented as the following (Kabir *et al.* 2008)

$$\tau(x) = Ce^{-\beta x} + \eta \quad (2)$$

where x is the distance from the cracked region, and C , β , η are constants obtained from the boundary conditions.

Assumptions used for current relations are described as the following:

1. Small deflection principle was considered in the analysis.
2. Mechanical behavior of adhesive and FRP was linear elastic.
3. No slippage between the FRP sheet and concrete substrate was considered.
4. Flexural stiffness of the concrete beam was assumed to be much higher than that of the FRP sheet.

5. In the analysis Euler-Bernoulli beam theory was applied, that is, plane sections remain plane and perpendicular to the neutral axis during bending.

In the previous researches considering the interfacial stresses in the FRP retrofitted RC beams, the main focus was on the interfacial bond stresses or adhesive between the FRP layer and the concrete substrate. However, in the present paper the main subject is the examination of interfacial concrete stresses at the vicinity of CFRP layer in the CFRP retrofitted RC beams. Interfacial part is introduced as a tensile part of the concrete adjacent to the CFRP layer. Experimental, finite element and theoretical solutions were carried out in order to obtain a better understanding of the effects of interfacial concrete stresses at the junction of concrete to CFRP layer. In the experimental process, strains on the concrete and the CFRP layer were measured. Strains on the interfacial concrete were measured till the concrete cracking. After the initiation of concrete cracking, strain gauges could not record any validate data on the tensile interfacial concrete. In addition, for a further extension of the research, a finite element modeling was validated with experimental results.

2. Experimental program

2.1 Materials

In the present research, six RC beams were prepared for monotonic testing from which three beams were retrofitted with CFRP fabrics. The concrete was a mixture of water, cement, sand and aggregate with the ratios (by mass) of: 0.55:1:2.2:1.7, respectively. The compressive strength of concrete using a series of standard cylindrical specimens of 150 mm in diameter and 300 mm in height was about 50 MPa at the date of testing the beams. The Typical geometry and reinforcement of the tested beams are illustrated in Fig. 1.

Longitudinal reinforcement with 12 mm diameter exhibited a yield stress of about 365 MPa and a Young modulus of about 205 GPa. Stirrups were made of steel bars with 10 mm diameter, yield stress of 260 MPa and young modulus of 180 GPa. The strengthening procedure was wet layup with two layer unidirectional CFRP sheets at the tension face of the concrete beam which

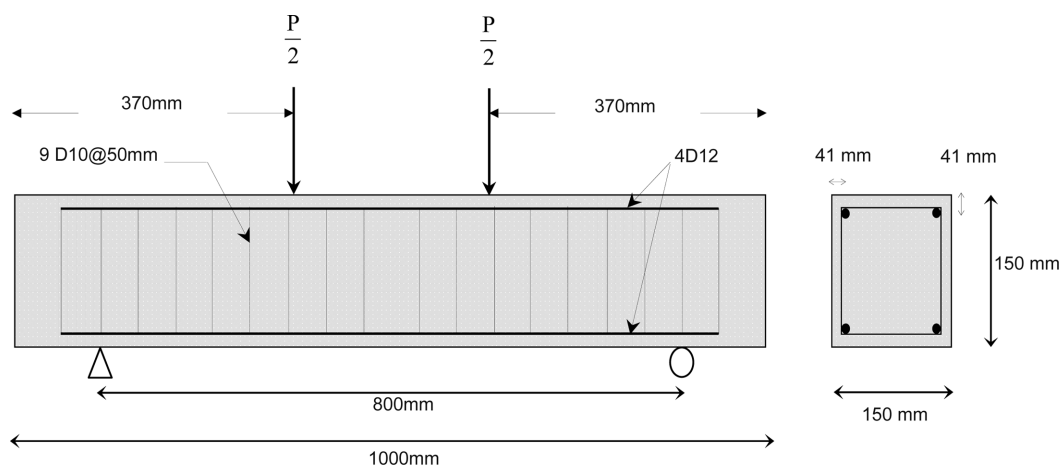


Fig. 1 Concrete beam geometry and reinforcement

Table 1 Mechanical properties of Carbon utilized fibers, CFRP composite and epoxy resin

	Tensile Strength (MPa)	Tensile Modulus of Elasticity (MPa)	Failure Strain (%)
Fibers	3900	230000	1.5
Epoxy Resin	45	3500	1.5
CFRP Composite	500	50000	1

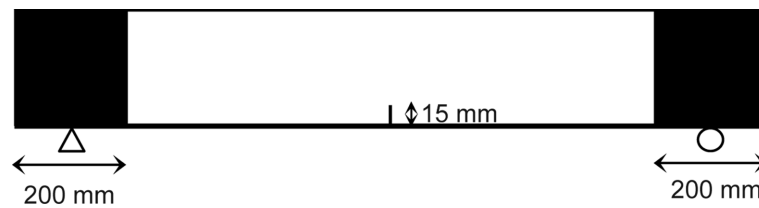


Fig. 2 Schematic presentation of the CFRP strengthened RC beam

strengthened the specimens in flexure. Further, U wrap CFRP sheets were implemented at the supports. The carbon fibers used in the CFRP sheets were Sika Wrap-200C and the utilized adhesive for bonding CFRP sheets to the concrete substrate was Sikadure-300 epoxy resin, all produced by the Sika company. The specifications of carbon fiber, epoxy resin, and assembled CFRP sheet are presented in Table 1.

A 15 mm deep notch was made at the middle bottom surface for all of the studied RC beams. The retrofitted specimens were strengthened with 2 layers of CFRP at the tension face of the specimens with a thickness of about 1 mm. The schematic presentation of the retrofitted RC beams is illustrated in Fig. 2.

2.2 Test setup

The instrument used for the testing was a servo-hydraulic universal testing machine. The beams were tested under four point bending and the mode of loading was displacement control with the rate of 0.005 mm/s.

In order to measure strains, strain gauges were mounted on the required locations of the specimens. Fig. 3 shows the test setup and strain gauges attached to the surface of the studied beams. Two types of strain gauges were used to record data. One kind of strain gauges used for the concrete which was the PFL type and the other used for the composite was the BFLA type, all from the TML, Japan company. Both of them had an electrical resistance of about 120 Ω . To collect strain gauges data, a static data logger TML type, Japan was used.

The collected data from the examined beams were used for load-deflection and strains at the critical regions. For all the specimens, one strain gauge was placed at the top surface of the RC beams to measure the compressive strains and the other two were mounted at the vicinity of the major flexural cracks positions already predicted from FE analysis. Three additional strain gauges were also positioned on the bottom of CFRP parallel to those attached on RC beam as shown in Fig. 4.

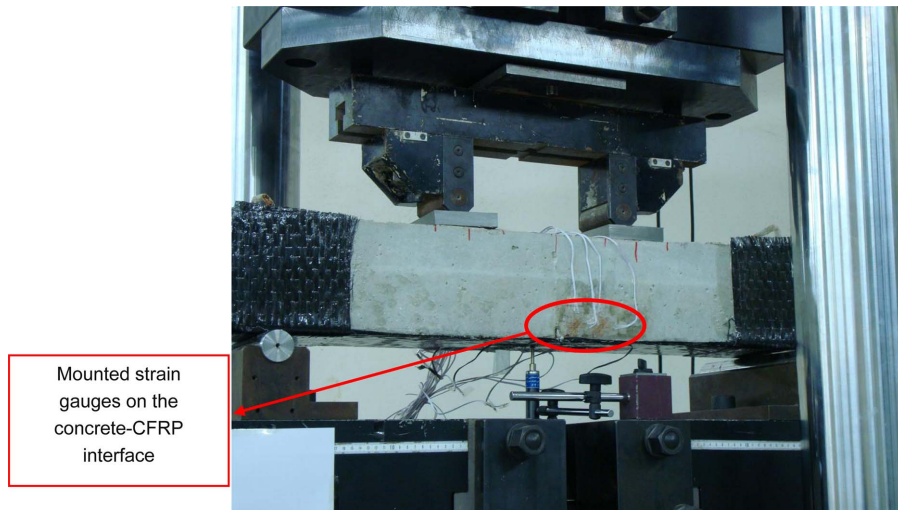


Fig. 3 Test set up arrangement

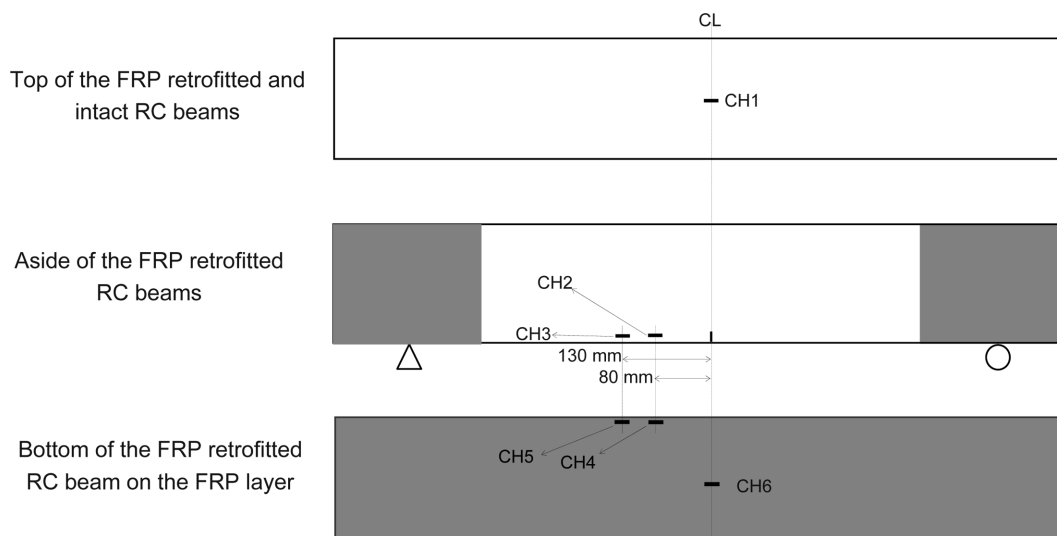


Fig. 4 Demonstration of the positions of mounted strain gauges

3. Finite element model

In order to verify the experimental test results, a numerical model using the finite element (FE) program ABAQUS was generated. The model used for concrete analysis was concrete damaged plasticity. Nonlinear compressive stress-strain relation used for the concrete was the model presented by Mander *et al.* (1988). It is a continuum, plasticity-based, damage model for concrete. It assumes that the two main failure mechanisms are tensile cracking and compressive crushing of the concrete material. The nonlinear model applied in the software is capable of elastic-isotropic modeling

including plastic isotropic-compressive and isotropic-tensile behavior.

The concrete mixture in the experimental program had a specific weight of approximately 2325 kg/m³. According to ACI 318-11 manual, the modulus of elasticity for normal weight would be calculated from the following equation

$$E_c = 4700\sqrt{f'_c} \quad (3)$$

This concrete modulus of elasticity was used in the FE software. For tensile behavior the model introduced by (Owen *et al.* 1983) was applied. According to ACI 318-11, the tensile strength or modulus of rupture is obtained from the following equation

$$f'_t = 0.7\sqrt{f'_c} \quad (4)$$

This value was introduced as the cracking stress in the tensile behavior model (Owen *et al.* 1983). The cracking strain was obtained by substituting the calculated parameters in to the equation below

$$\varepsilon'_t = 1.8(f'_t/E_c) \quad (5)$$

This yielded a cracking strain of 0.00027. It should be noted that according to the tensile behavior model (Owen *et al.* 1983) in the FE analysis after cracking initiation, the tensile stress decreased and became equal to zero at a tensile strain of about $12\varepsilon'_t$, and this was used in the software. For the steel rebar, input data for isotropic elastic-perfectly plastic behavior of the material included the modulus of elasticity and the yield stress.

A two layer CFRP sheet was connected to the tensile side for which a linear behavior was considered in the FE analysis.

Convergence of the FE analysis was mesh sensitive. Mesh sizes were specified so that the analysis not be time consuming, the convergence could be facilitated, and also the optimum precision of results could be obtained.

Elements used for the concrete were the 8 node brick C3D8R type with the size of 20 mm and the totals number of 6270. Concrete elements were fined to the size of 3.6 mm around the crack.

The cracked part at the middle section of the beam was modeled as a flaw. Considering the meshes at other parts of the beam with the dimensions of $14 \times 14 \times 18$ mm, meshes were fined at the cracked middle section of the beam with reducing the dimensions to $3.5 \times 1.8 \times 18$ mm. For concrete elements the option Reduced Integration was selected so that the convergence of nonlinear FE analysis of the concrete elements would be facilitated.

For the CFRP layer, 4 node shell elements named S4R were applied with the size similar to the concrete and the total number of 450. Finally, 2 node 3D truss elements named T3D2 with the total number of 540 elements were applied for steel rebar.

Interactions which were constraints between parts of the specimens applied in the software, consisted of contact behavior between grips and top surface of the concrete. Also, the CFRP layer was tied to the concrete surface. In addition, by using the software feature named embedded region, interaction between steel rebar and concrete was performed. Fig. 5 demonstrates the FE model.

In order to present a verification for the experimental and numerical results, a simple theoretical solution was carried out. Assumptions considered for the current analysis are listed below:

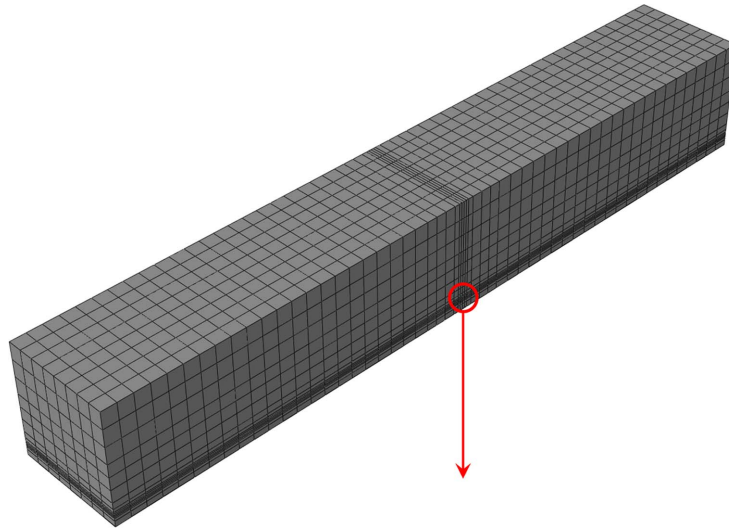


Fig. 5(a) The finite element model

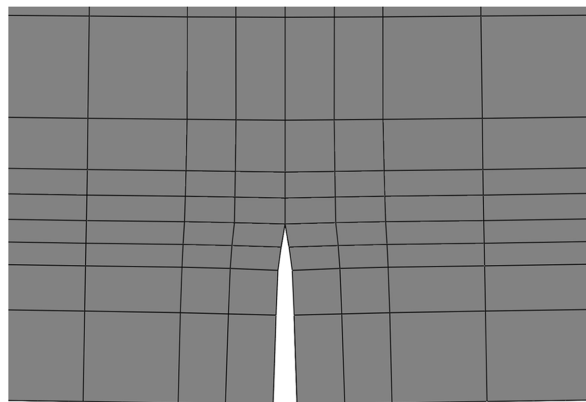


Fig. 5(b) Fined mesh around the crack tip in RC beam FE modeling

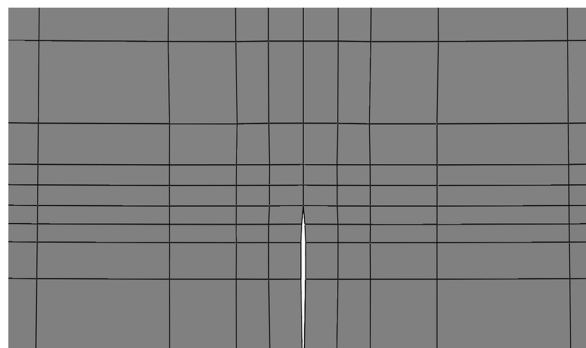


Fig. 5(c) Fined mesh around the crack tip in CFRP retrofitted RC beam FE modeling

1. Small deflection principle was considered in the analysis.
2. Mechanical behavior of the CFRP layer was linear elastic.
3. No slippage between CFRP sheet and concrete substrate was considered.
4. No slippage between steel rebar and concrete was considered.
5. In the analysis Euler-Bernoulli beam theory was applied.
6. Strain compatibility assumption between the CFRP sheet, steel rebar and concrete was considered.

Relations between recited strains on the concrete at the concrete-CFRP interface and the total applied load, up to the concrete cracking, were generated. Strains compatibility and stresses diagram at the location of channels 2,3,4,5 (illustrated in Fig. 4) are shown in Fig. 6. Considering strain compatibility amongst the rebar, concrete and CFRP sheet, parameters presented in the Figure would be defined as the following:

- ϵ_{CC} is strain of compressive top surface of the concrete
- ϵ_{CT} is strain at the location of mounted strain gauge on the tensile concrete
- ϵ_{SC} is strain of the compressive steel rebar
- ϵ_{ST} is strain of the tensile steel rebar
- ϵ_{FRP} is strain of the tensile CFRP sheet
- c is distance from neutral axis to the top surface of the beam

Other parameters presented in Fig. 6 are distances from centroid of the elements to the top surface of the beam.

In this case the solution was up to the cracking of the tensile concrete, thus, all the elements behave linearly and with the strain compatibility assumption, all the strains as a linear function of ϵ_{SG} could be organized as the following

$$\epsilon_{CC} = \frac{c}{140-c} \epsilon_{CT}$$

$$\epsilon_{SC} = \frac{c-41}{140-c} \epsilon_{CT}$$

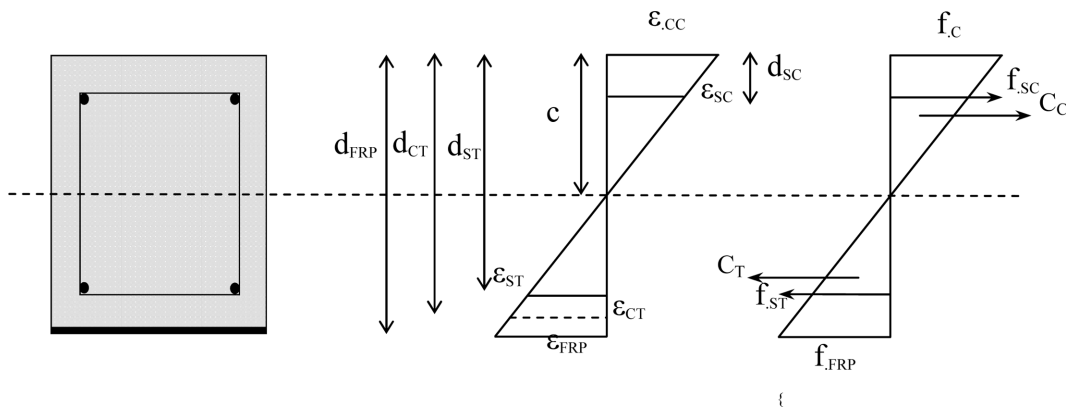


Fig. 6 Strains compatibility and stress diagrams of elements of the CFRP retrofitted RC beam before the concrete cracking

$$\begin{aligned} \varepsilon_{ST} &= \frac{109-c}{140-c} \varepsilon_{CT} \\ \varepsilon_{FRP} &= \frac{150.5-c}{140-c} \varepsilon_{CT} \end{aligned} \tag{6}$$

From the forces equilibrium equation at the strain gauge location, the value of c was defined. With respect to the strain compatibility relations, replacing the calculated c into the section moment equation the following linear relations between applied load and strains on the tensile concrete ε_{CT} (channels 2,3 in Fig. 4) and strains on the CFRP (channels 4,5 in Fig. 4) up to the tensile concrete cracking achieved as

$$\varepsilon_{CT} (\mu s) = 6.53 \times P \text{ (kN)} \tag{7}$$

$$\varepsilon_{FRP} (\mu s) = 7.6 \times P \text{ (kN)} \tag{8}$$

Another theoretical verification presented was for the relation between strains on the CFRP (channels 4,5 in Fig. 4) and loading up to the failure of the specimen. Obviously in this situation, the stress-strain of concrete was nonlinear after the cracking and the modified Hognestad model (Macgregor 2000) was used.

The parameters were similar to those of the linear solution. Strain compatibility amongst the rebar, concrete and CFRP sheet and stresses in the mentioned parts, are illustrated in Fig. 7. at the cracked section of the beam, concrete had nonlinear behavior and the tension part was neglected. Similar to the previous session, in order to obtain a relation between applied load and strain in the FRP, the force and moment equilibrium equations at the cracked section were required to be solved simultaneously as the following:

$$C_c + f_{SC}A_{SC} - f_{ST}A_{ST} - f_{FRP}A_{FRP} = 0 \tag{9}$$

$$C_c \times \bar{y} + f_{ST}A_{ST}(d_{ST} - c) + f_{SC}A_{SC}(c - d_{SC}) + f_{FRP}A_{FRP}(d_{FRP} - c) = M_T(x) \tag{10}$$

Where C_c and \bar{y} , are the overall compression force in the pressure concrete and its centroid distance from the neutral axis, respectively. A parametric solution of C_c and \bar{y} was defined by integration on the concrete depth as the following

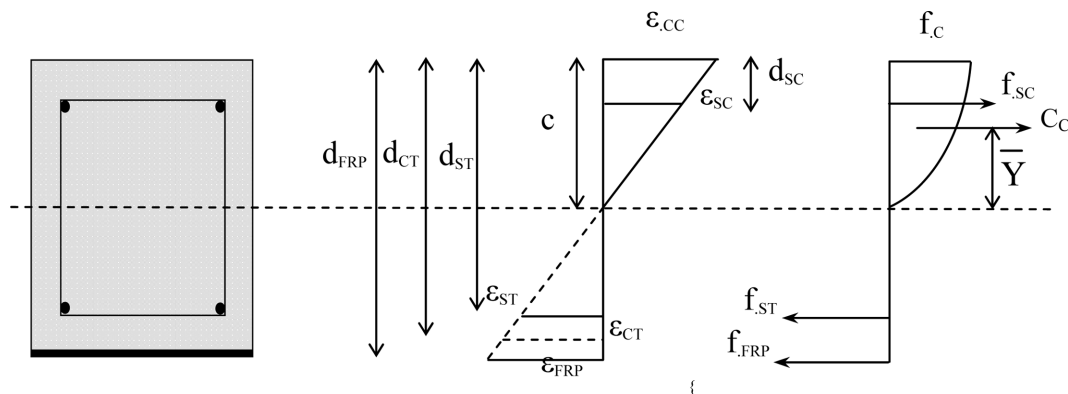


Fig. 7 Strains compatibility and stress diagrams of elements of the CFRP retrofitted RC beam after the concrete cracking

$$C_c = \int_0^c \omega_c \cdot f_{cc} \left[2 \frac{y \varepsilon_c}{c \varepsilon_{c0}} - \left(\frac{y \varepsilon_c}{c \varepsilon_{c0}} \right)^2 \right] dy = \omega_c f_{cc} \left[c \frac{\varepsilon_c}{\varepsilon_{c0}} - c \frac{\varepsilon_c^2}{3 \varepsilon_{c0}^2} \right] = c \omega_c f_{cc} \frac{\varepsilon_c}{\varepsilon_{c0}} \left[1 - \frac{\varepsilon_c}{3 \varepsilon_{c0}} \right] \quad (11)$$

$$\begin{aligned} \bar{y} &= \frac{\int_0^c y \omega_c f_{cy} dy}{C_c} = \frac{\int_0^c \omega_c f_{cc} \left[2 \frac{y^2 \varepsilon_c}{c \varepsilon_{c0}} - y^3 \left(\frac{\varepsilon_c}{c \varepsilon_{c0}} \right)^2 \right] dy}{C_c} \\ &= \frac{\omega_c f_{cc} \left[2 \frac{c^2 \varepsilon_c}{3 \varepsilon_{c0}} - \frac{c^2}{4} \left(\frac{\varepsilon_c}{\varepsilon_{c0}} \right)^2 \right]}{C_c} = \frac{c^2 \omega_c f_{cc} \left[\frac{2}{3} - \frac{1}{4} \frac{\varepsilon_c}{\varepsilon_{c0}} \right]}{c \omega_c f_{cc} \frac{\varepsilon_c}{\varepsilon_{c0}} \left[1 - \frac{1}{3} \frac{\varepsilon_c}{\varepsilon_{c0}} \right]} = \frac{\frac{2}{3} - \frac{1}{4} \frac{\varepsilon_c}{\varepsilon_{c0}}}{1 - \frac{1}{3} \frac{\varepsilon_c}{\varepsilon_{c0}}} \end{aligned} \quad (12)$$

Were, ω_c is the beam width, ε_{c0} is the peak strain in stress-strain diagram of the compressive concrete, ε_c is compressive concrete strain, and f_{cc} is the compressive strength of concrete.

Thus, with a distinct value of applied force, and using the compatibility relations as mentioned in Eq. (3), solving the nonlinear Eqs. (6) and (7) resulted in the value of c . Finally the unknown value of the FRP strain was calculated.

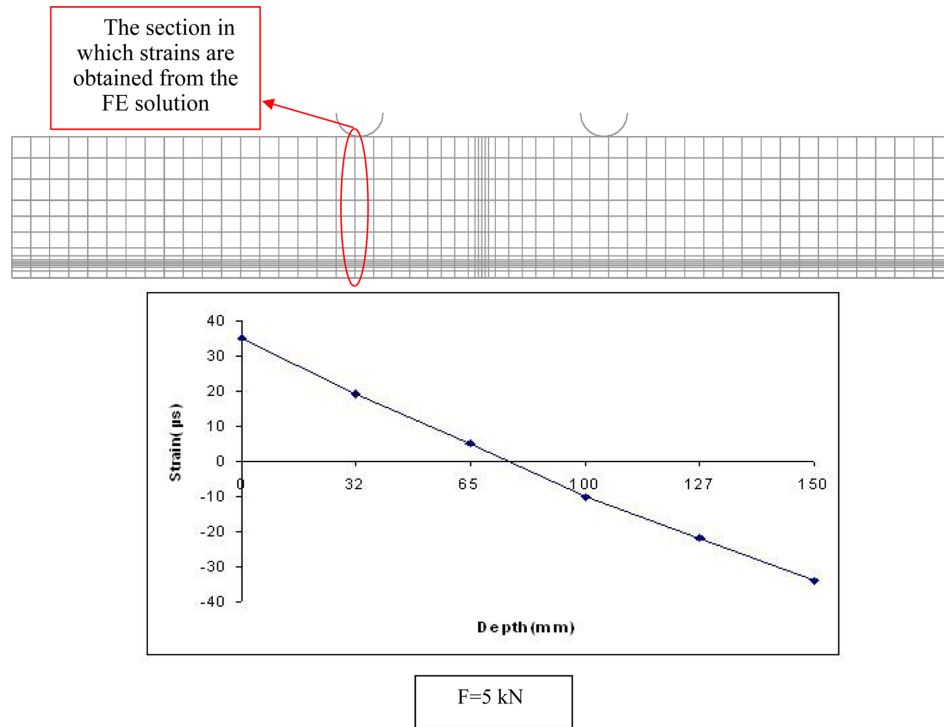
4. Results and discussions

First, a numerical solution on the strain distribution along the beam depth in an arbitrary section of the CFRP retrofitted RC beam is illustrated in Fig. 8. The result here can verify the strain compatibility assumption used previously.

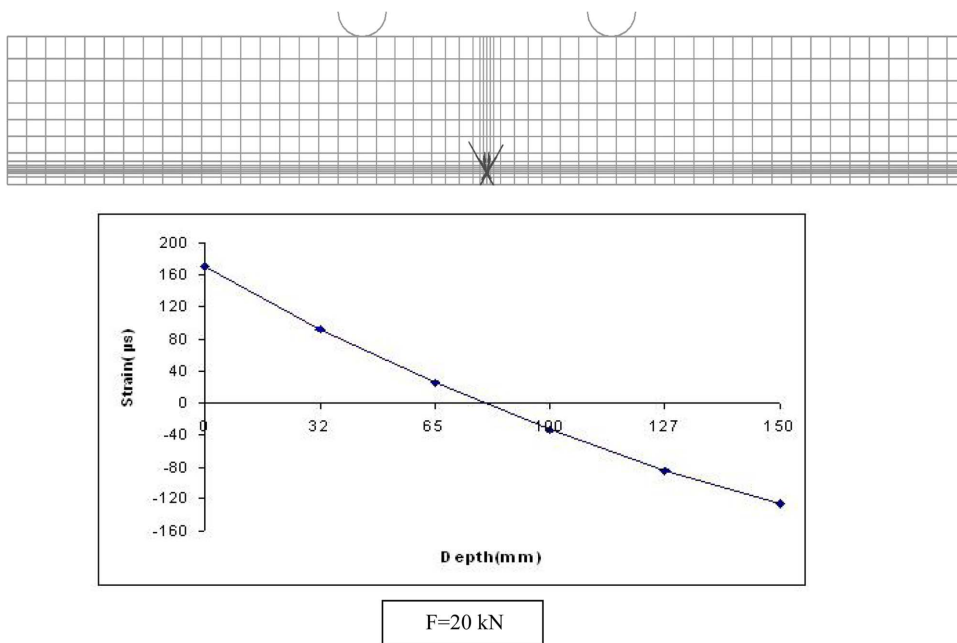
One should notice that in the FE modeling of concrete by ABAQUS package, plastic strains indicate cracked elements. From the Fig. 8 it can be observed that with the applied load growth the crack evolution continued. Also, increase of the strains, specially plastic strains, resulted in changes of neutral axis position.

Fig. 8 also describes cracks distribution and progressive damage of FE model of retrofitted specimens. As can be seen, at the very early steps of loading cracking initiated at the tip of the notch which is shown in Fig. 8(b). Then, with the increase of loading crack distributed along the beam to the location of grips as illustrated in Fig. 8(c). Also, after steps of loading, cracks distributed along the beam and also reached to the top of the beam. At the failure, distribution of cracks at the top surface depicted compressive concrete crushing as can be seen in Fig. 8(f). Furthermore, at this level of loading, yield of tensile steel rebar occurred.

The load-deflection diagrams of the control and CFRP strengthened beams are illustrated in Fig. 9 along with those estimated by FE analysis. As can be noticed from these Figure, although the use of the 2 layer CFRP fabric decreased the ductility of the intact RC beams but led to the increase of the load carrying capacity of about 75%. Furthermore, the initial observed slope changes of the load-deflection diagrams are attributed to the stiffness change originated from the initial crack formation at the tip of the pre-cracked section of the beams as well as the bottom of the grips. The magnitudes of these slopes were about 64 kN/mm and 45 kN/mm for the CFRP and intact beams, respectively. The second slope changes observed in Fig. 9 is related to the yielding of the rebar. The comparison

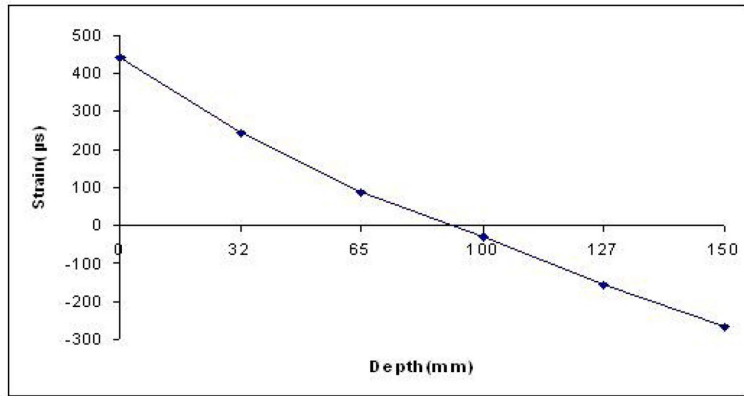
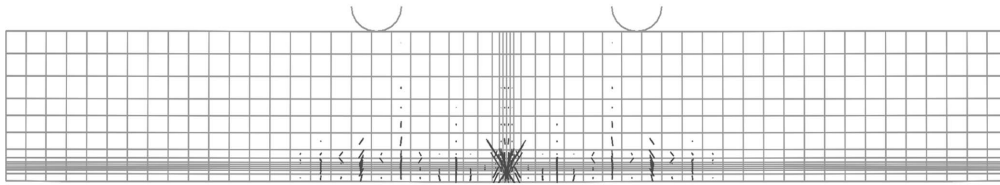


(a)



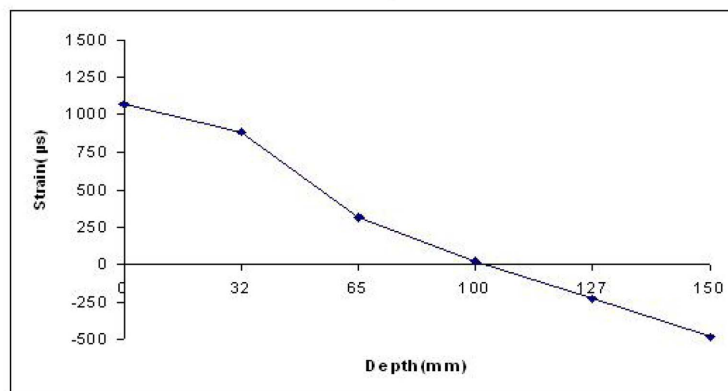
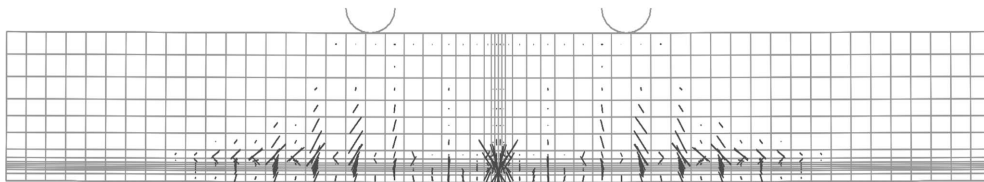
(b)

Fig. 8 Strain distribution across depth in an arbitrary section of CFRP retrofitted RC beam resulted from the FE solution



F=30 kN

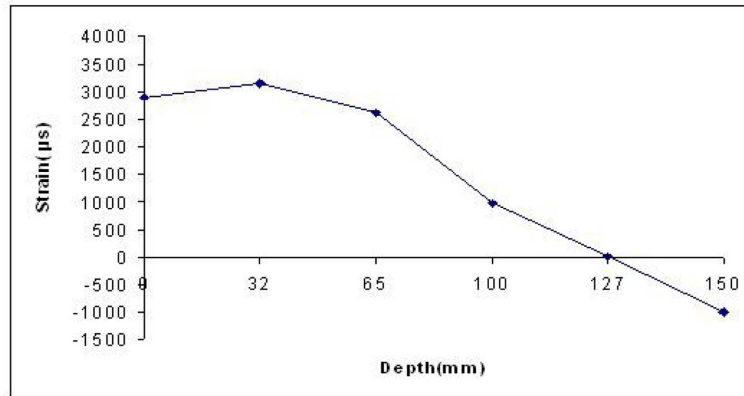
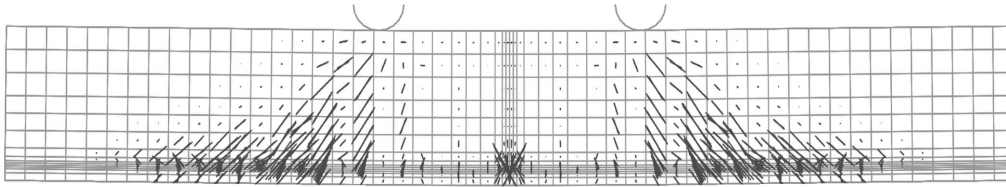
(c)



F=50 kN

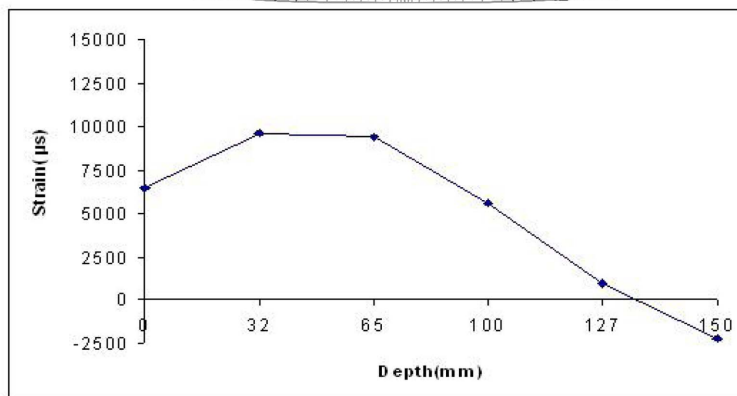
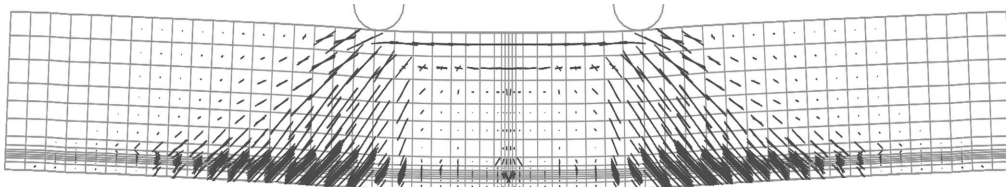
(d)

Fig. 8 Continued



F=120 kN

(e)



F=200 kN

(f)

Fig. 8 Continued

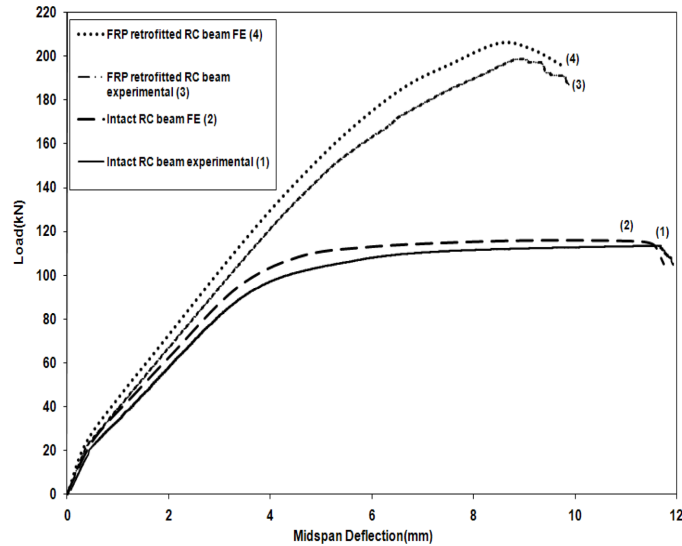


Fig. 9 Load-deflection curves for intact and CFRP retrofitted RC beams

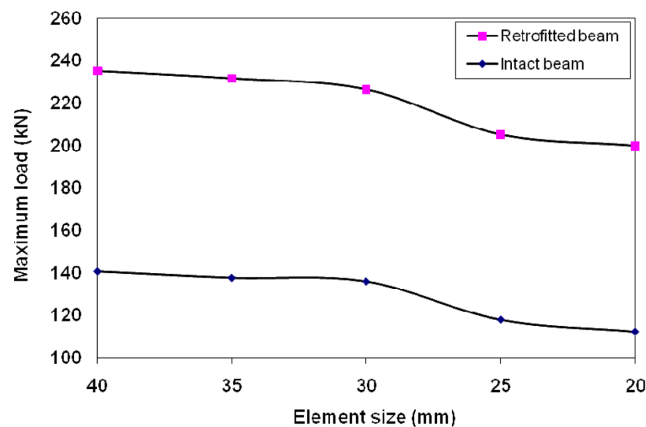


Fig. 10 Load carrying capacity versus elements size in the FE analysis

of both sets of slope changes for these two beams suggests a more plastic deflection behavior in case of CFRP beam. Moreover, FE analysis also revealed a rather non-linear behavior for the deflection load variations of the plastic part in agreement with experimental data.

On the FE modeling convergence results a description is presented. As mentioned earlier, the FE analysis results were mesh sensitive and in the proceeding diagram, load versus number of elements applied in the analysis is shown. In this parametric study, effect of the concrete element size on the load obtained was examined. The use of concrete elements with the size of 20 mm resulted in an optimized load carrying capacity for Intact RC beams of 116 kN and for CFRP retrofitted RC beams of 206 kN. Increase of the mentioned size resulted in the decrease of maximum loads till constant values which were close to the experimental ones. In Fig. 10 concrete elements sizes are depicted for which number of elements varied from 500 to 6270.

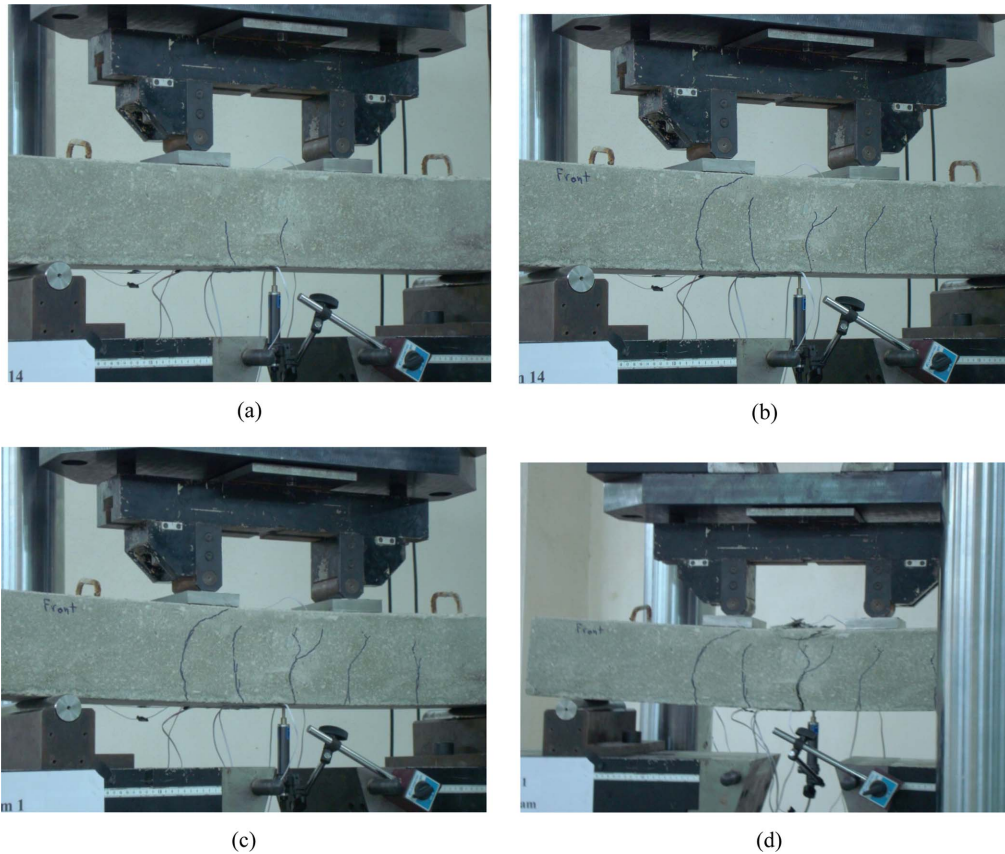


Fig. 11 Cracking, damage progress and failure in an intact RC beam. (a) $P = 20$ kN, (b) $P = 60$ kN, (c) $P = 100$ kN, (d) $P = 113$ kN

Fig. 11 describes progressive damage during stages of experimental monotonic loading of intact RC specimens. As can be observed from this Figure with the progression of monotonic loading, cracks were distributed. First crack initiation was at the tip of the notch and almost at the same time at the location of the bottom of grips other cracks began to propagate. At the notch tip crack began to spread in two directions as illustrated in Fig. 11(b). In the intact RC beams, almost all cracks distributed along beam between the two grips. Cracks propagated to the top surface of the specimens till the failure when compressive concrete crushing occurred as shown in Fig. 11(d).

Fig. 12 describes progressive damage during stages of monotonic loading of CFRP retrofitted RC specimens. With the increase of loading, cracks distributed along the beam. At the early stages of loading crack propagation and initiation started at the location of the notch tip and beneath the grips almost simultaneously. Crack at the notch tip was observed to propagate in a unique direction as illustrated in the Fig. 12. Considering the comparison of cracks distribution of CFRP retrofitted RC beams to the intact RC beams, it can be observed that not only more cracks initiated and propagated with the increase of loading, but also cracks distributed along the whole beam length. In addition, it can be seen that because of existence of the CFRP sheet, crack propagation at the notch tip was less than that of the intact RC specimens. With the progression of loading stages, produced cracks

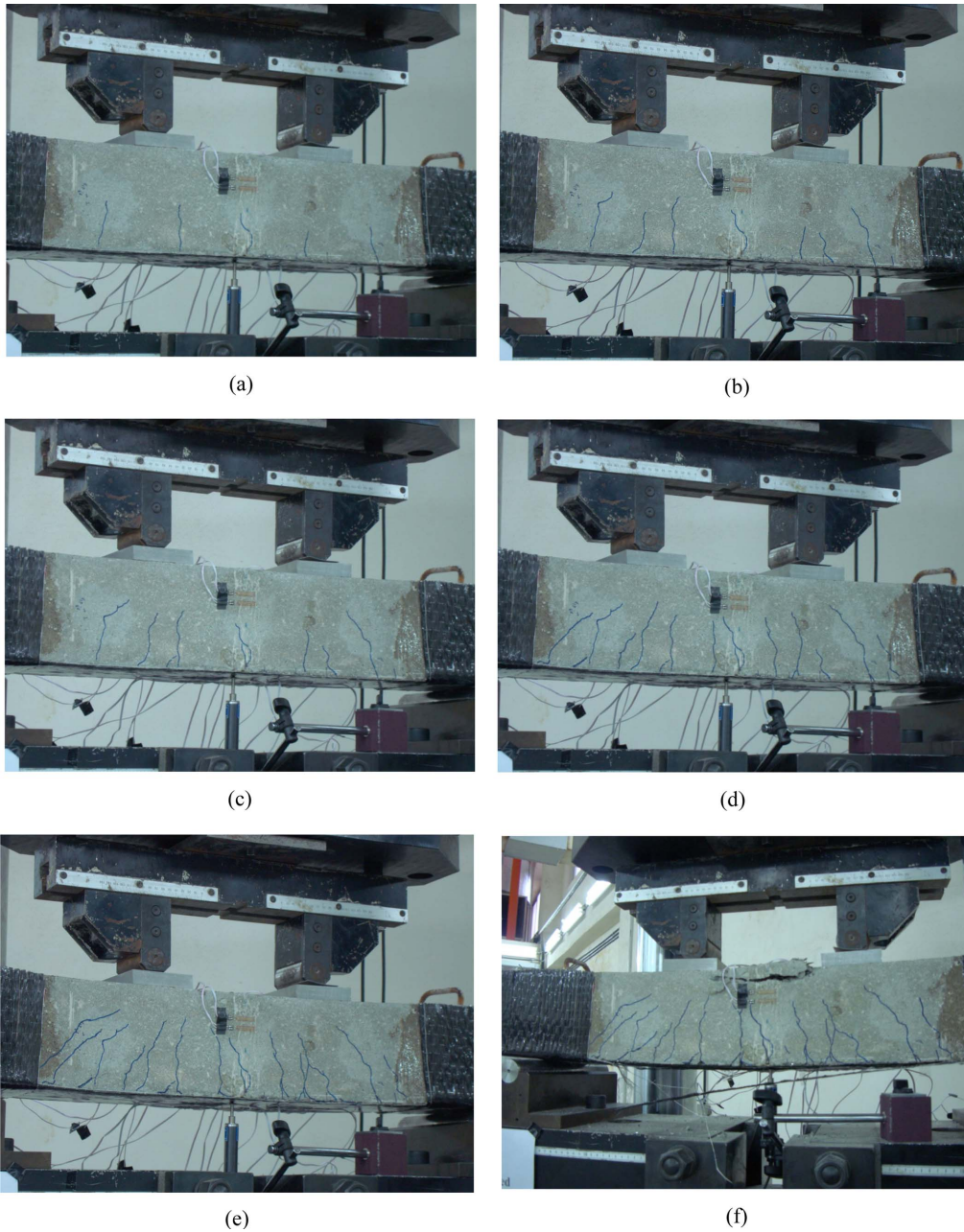


Fig. 12 Cracking, damage progress and failure in an intact RC beam. (a) $P = 50$ kN, (b) $P = 100$ kN, (c) $P = 120$ kN, (d) $P = 150$ kN, (e) $P = 180$ kN, (f) $P = 198.6$ kN

propagated to the top surface of the specimens till the failure as illustrated in Fig. 12(e). At the failure of the retrofitted beams modes of failure including compressive concrete crushing and the CFRP sheet rupture occurred almost simultaneously as shown in Fig. 12(f).

Figs. 13 to 16 display crack patterns obtained based on experimental test and FE analysis for the

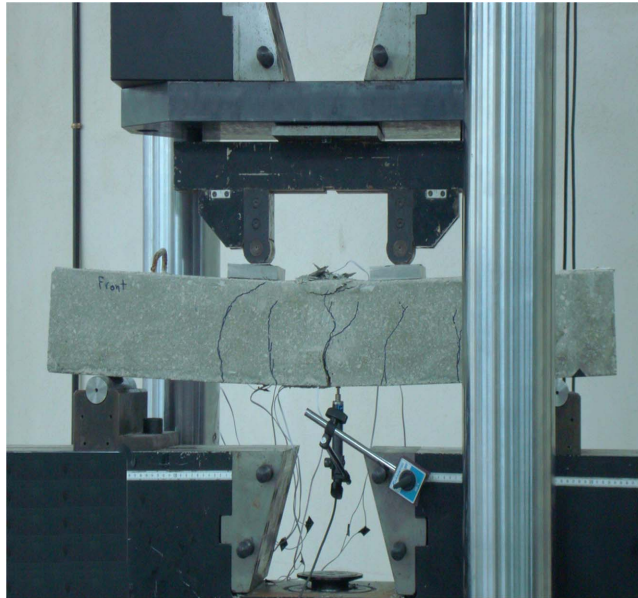


Fig. 13 Cracking pattern from the experimental test in a RC control beam at the failure

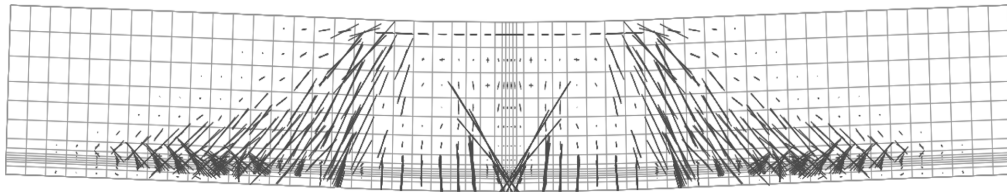


Fig. 14 Cracking pattern from the FE in a RC control beam at the failure

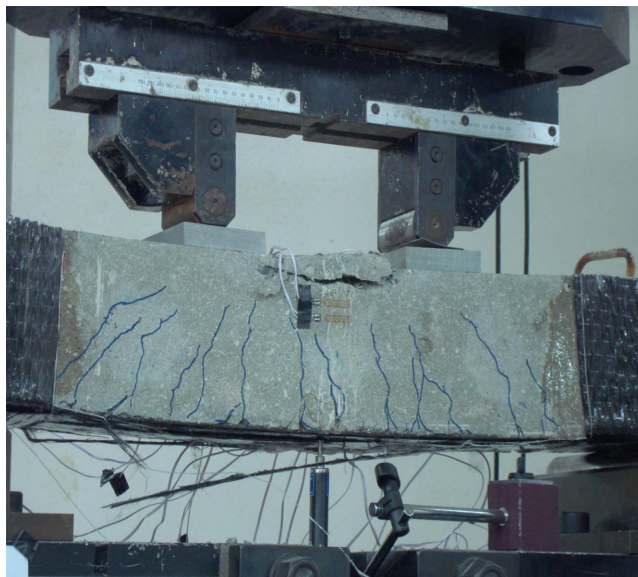


Fig. 15 Cracking pattern from the experimental test in a CFRP retrofitted RC beam at the failure

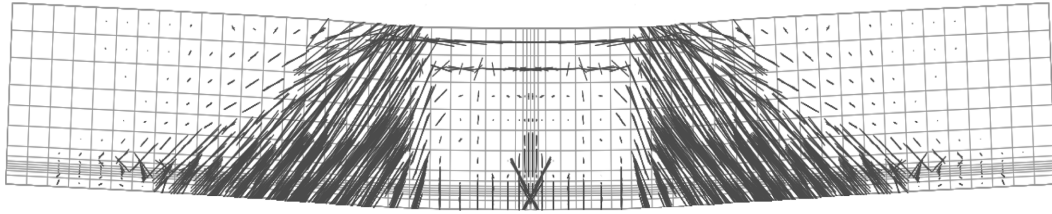


Fig. 16 Cracking pattern from the FE in a CFRP retrofitted RC beam at the failure

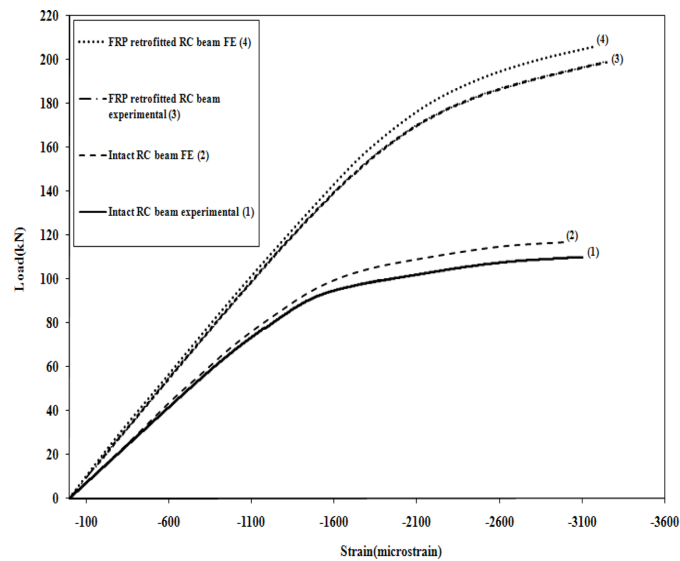


Fig. 17 Strains of the compressive concrete at channel1 for the intact and CFRP retrofitted RC beams

intact and CFRP beams, respectively. As can be noticed from these patterns, the formation of larger numbers of cracks for the latter could be verified compared to those of the intact beams despite the applying similar loading conditions. Existence of more distributed flexural cracks along the beam can be clearly observed for the CFRP beams in comparison with those of intact beams.

In Fig. 17, load versus compressive concrete strain obtained from the channel 1 is illustrated. Experimental results are verified with the FE ones. As can be seen, with the increase in the load carrying capacity the crushing strain of the specimens was about $-3300 \mu s$.

Strains on the concrete at the junction zone of the CFRP-concrete at the tension part of the CFRP retrofitted RC beam, resulted in the interfacial stresses between the CFRP layer and the concrete. It should be noted that the measurement of such strains was difficult because of the brittleness of concrete, and any discrete crack caused the gauges work improperly.

The gauges on the interfacial tensile concrete were mounted at the vicinity of the major flexural cracks. These locations were predicted using the finite element analysis. These gauges that were, CH2 (channel 2) and CH3 (channel 3), were functional until the flexural cracks began to propagate. Figs. 18 to 24 show strains at these zones on the concrete and its corresponding location on the CFRP layer at CH4,5 (means channels 4 and 5). Strains of CH4 and CH5 and CH6 on the CFRP, till the failure of the specimens, are also illustrated.

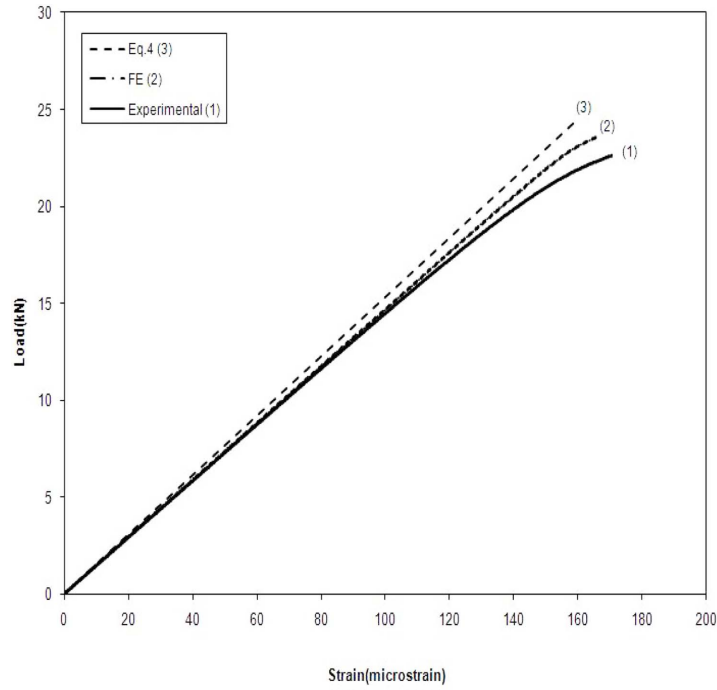


Fig. 18 Strains at the channel 2 on the tensile concrete at the CFRP-concrete interface, at the range of concrete cracking

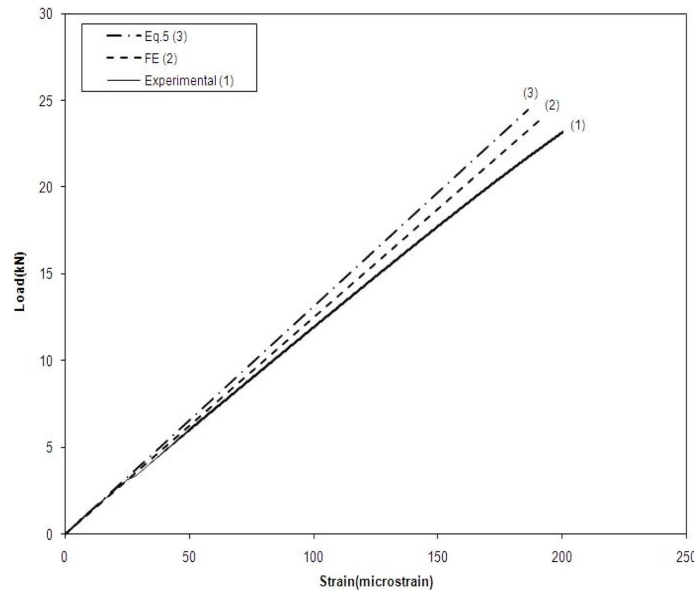


Fig. 19 Strains at channel 4 on the CFRP at the range of concrete cracking, for the CFRP retrofitted RC beams

The preceding results were obtained from the experimental measurement, FE analysis and a calculation using equilibrium equation and strain compatibility at the locations of channels 2-5. For the concrete here, the tensile strength (or the rupture modulus) was 4.5 MPa, and the corresponding strain was about $160 \mu\epsilon$.

Figs. 18 and 19 show the variations of the applied load versus strain for the CFRP retrofitted RC beams for which the strain data were collected from the strain gauges mounted on the concrete and on the CFRP, which were channels 2,4, respectively. Further, the calculated variations of the strains appearing at the interface and the CFRP before cracking are also shown in Figs. 18 and 19 using Eqs. (4) and (5) as well. As can be noticed from these Figures, rather discrepancy can be noticed between the calculated data trend and those of the experimental and the FE. The observed slight non-linearity could be related to the brittle manner of concrete and spreading of the micro-cracks at the very initial steps of loading. In Fig. 18 the slope change was resulted from the crack initiation at the middle section of the beams and at the location of the strain gauges on the concrete which happened almost simultaneously at the load of about 25 kN. Fig. 20 show the crack initiation in the CFRP retrofitted RC specimens from the FE analysis.

In Fig. 21, strains in the CFRP at channel 4 at the range of the specimen failure is presented. Experimental and FE solution are compared with each other. The first change in the slope indicates the crack initiation which as mentioned earlier happened at the load of 25 kN that was at the very

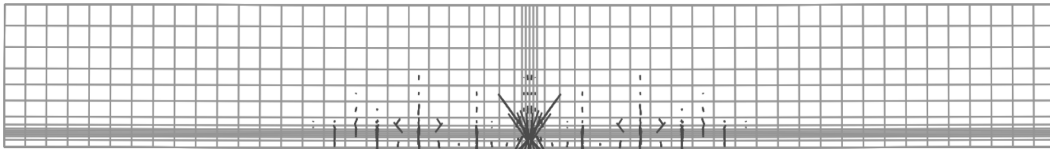


Fig. 20 Crack initiation in the CFRP retrofitted RC beams from the FE solution

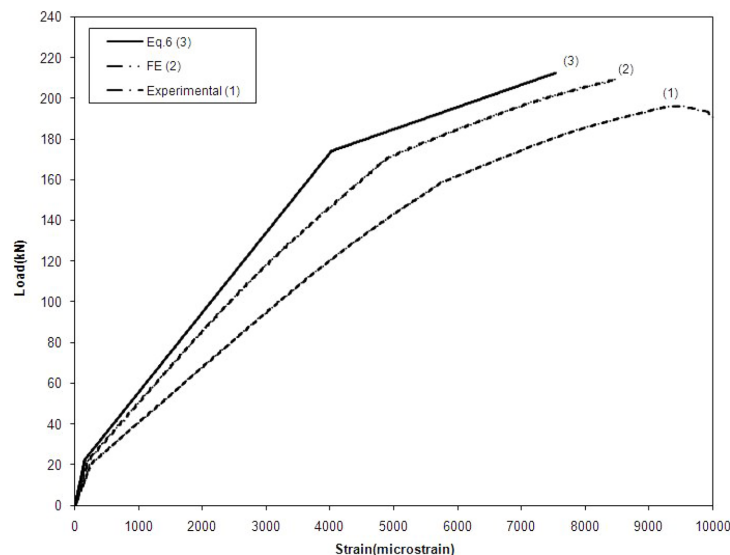


Fig. 21 Strains at channel 4 on the CFRP at the range of specimen failure, for the CFRP retrofitted RC beams

first steps of loading. The second change in the slope is due to the yielding of longitudinal steel rebar.

Fig. 18 Strains at the channel 2 on the tensile concrete at the CFRP-concrete interface, at the range of concrete cracking

In Figs. 22 and 23 variations of the strains appearing at the interface and the CFRP before cracking are shown. Fig. 24 illustrates load versus strain on the CFRP at the channel 5 at the range

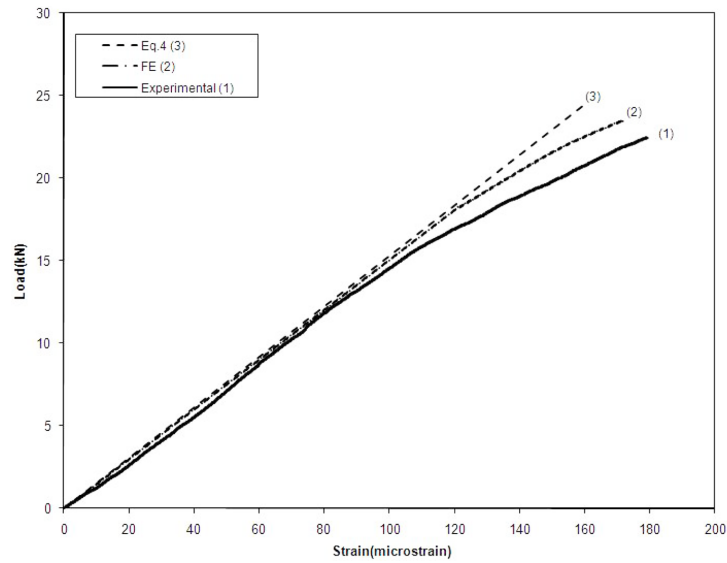


Fig. 22 Strains at the channel 3 on the tensile concrete at the CFRP-concrete interface, at the range of concrete cracking

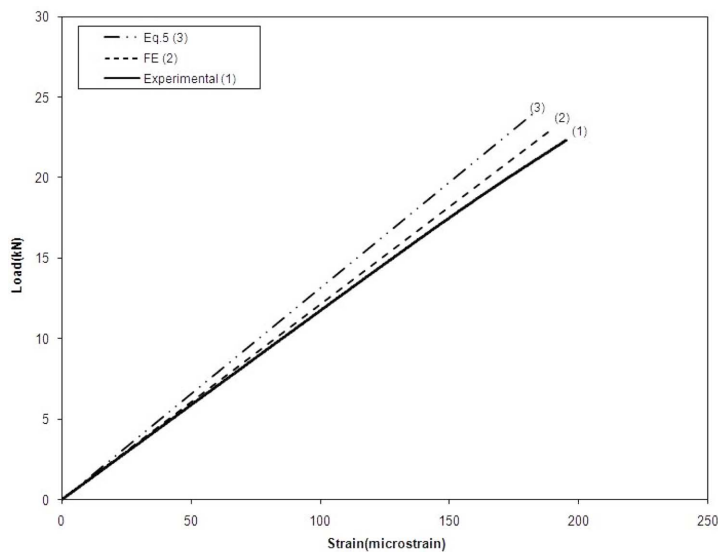


Fig. 23 Strains at the channel 5 on the CFRP, at the range of concrete cracking

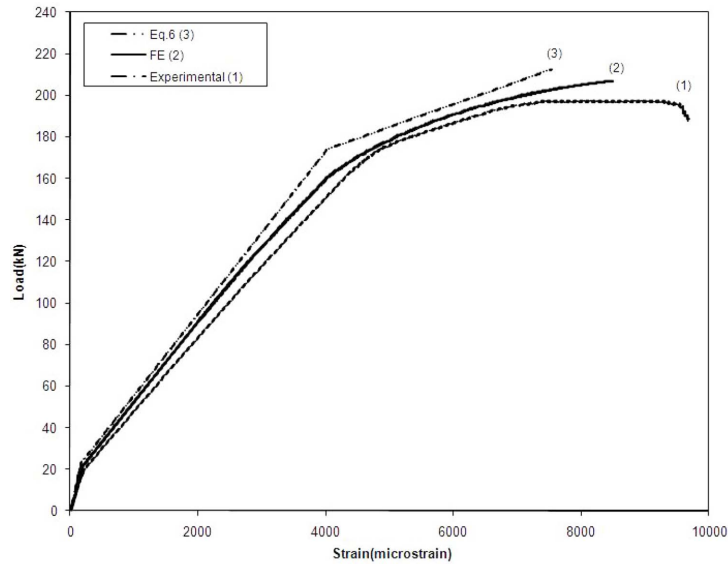


Fig. 24 Strains at the channel 5 on the CFRP, at the range of specimen failure

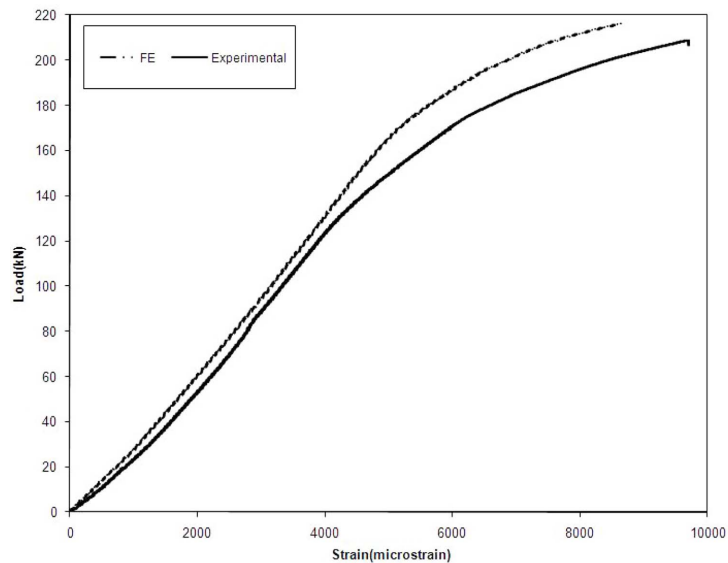


Fig. 25 Strains at the channel 6 on the CFRP at the range of specimen failure

of the specimen failure. Again, change in the slope is observed at the cracking initiation of the specimen and at the yielding of the longitudinal steel rebar.

Fig. 25 shows the load versus strain resulted from strain gauge channel 6. Strain gauge ch6 (referring to Fig. 4) was placed on the CFRP layer at the pre-cracked middle section of the retrofitted specimens. As can be observed, the initial slope here is much higher than that of load-strain illustrations of channels 4 and 5 shown in Figs. 21 and 24. This is because of the existence of

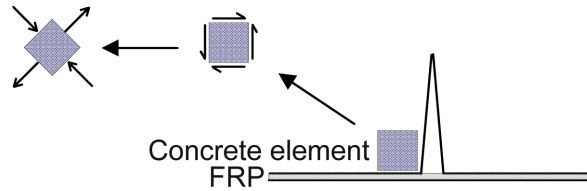


Fig. 26 Interfacial concrete element at the vicinity of a crack

the notch at the middle section of specimens. The mentioned notch with the depth of 15 mm (as illustrated in Fig. 2) caused another phenomenon that can be observed in Fig. 25. At the early stages of loading, a hardening behavior can be seen in the load-strain curve in Fig. 25, and that would be resulted from the notch located at the mid-span between FRP layer and the concrete substrate. At the very beginning steps of loading, tensile stresses spread through the mentioned notch till they reached to the tip. Proceeding such path from the crack opening initiation till damaging process at the crack tip caused the variation of slope of load-strain relationship for the strain at ch6 on CFRP layer behave increasingly at the early steps of loading. Consequently, hardening behavior can be observed in Fig. 25.

The measured load-strain behavior on the CFRP sheet up to the interfacial concrete cracking was almost linear. However, this relation on the interfacial concrete exhibited a slight nonlinearity which was because of the brittle manner of the concrete and spreading of the micro-cracks at the very initial steps of loading. In the following, a discussion is proposed about the situation of the interfacial concrete at the vicinity of cracks.

As can be seen in Fig. 26, an interfacial concrete element near a distributed discrete crack which was also at the vicinity of the CFRP layer, experienced a pure shear stress resulted from the tensile force in the CFRP sheet. Simply, there was compressive and tensile stresses on the concrete element.

From the measured strains along the CFRP sheet, a mean shear interfacial stress can be computed between two consecutive gauge positions. Given two strain readings g_i and g_j at positions i and j , the laminate thickness t_p , its elastic modulus E_p , and the distance Δl_{i-j} between the two gauge positions (i refers to the channel 4 and j refers to the channel 5), the average shear stress, τ_{i-j} , between the gauges can be determined as follows (Bizindavyi *et al.* 1999)

$$\tau_{i-j} = \frac{t_p \cdot E_p \cdot (g_i - g_j)}{\Delta l_{i-j}} \quad (13)$$

An assumption considered for the current relation was that no slippage between the CFRP sheet and concrete substrate was considered.

Considering the relation above, for the channels 4 and 5 on the CFRP sheet, the mean shear stress at the final steps of the loading was about 2 MPa which as much less than the tensile strength of the concrete. This means that there was no possibility for debonding between the grips. The interfacial debonding failure was inevitable if interfacial cracks reached 45° in direction and stresses approached the tensile concrete strength, simultaneously.

Fig. 27 illustrates the FE solution of crack evolution in a RC control beam. As can be seen from the Fig. 27(a) cracking initiation was at the pre-cracked middle section of the beam. After little stages of loading other cracks initiated from the beneath of grips which is shown in Fig. 27(b). With

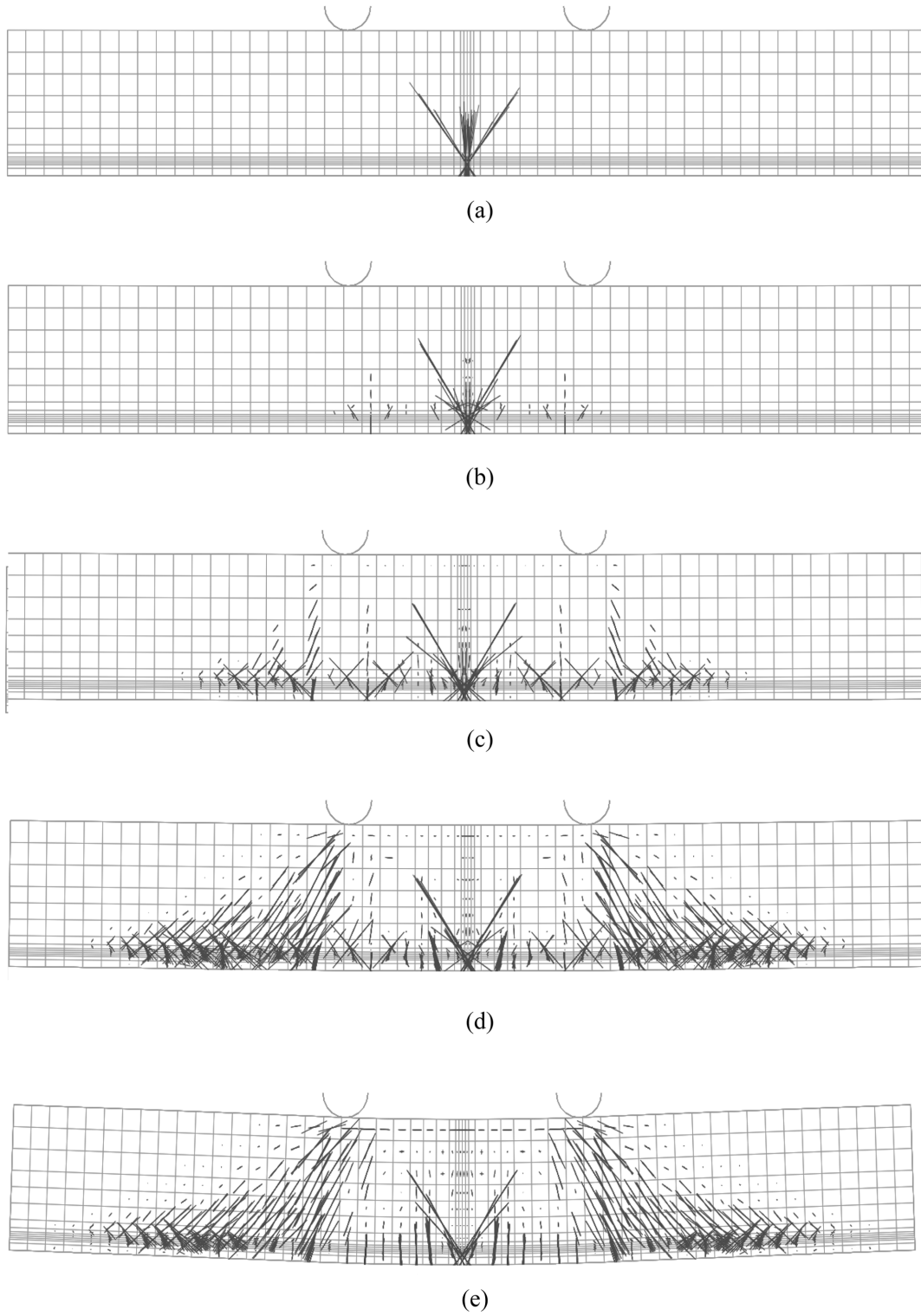


Fig. 27 FE solution of crack evolution in RC control beam

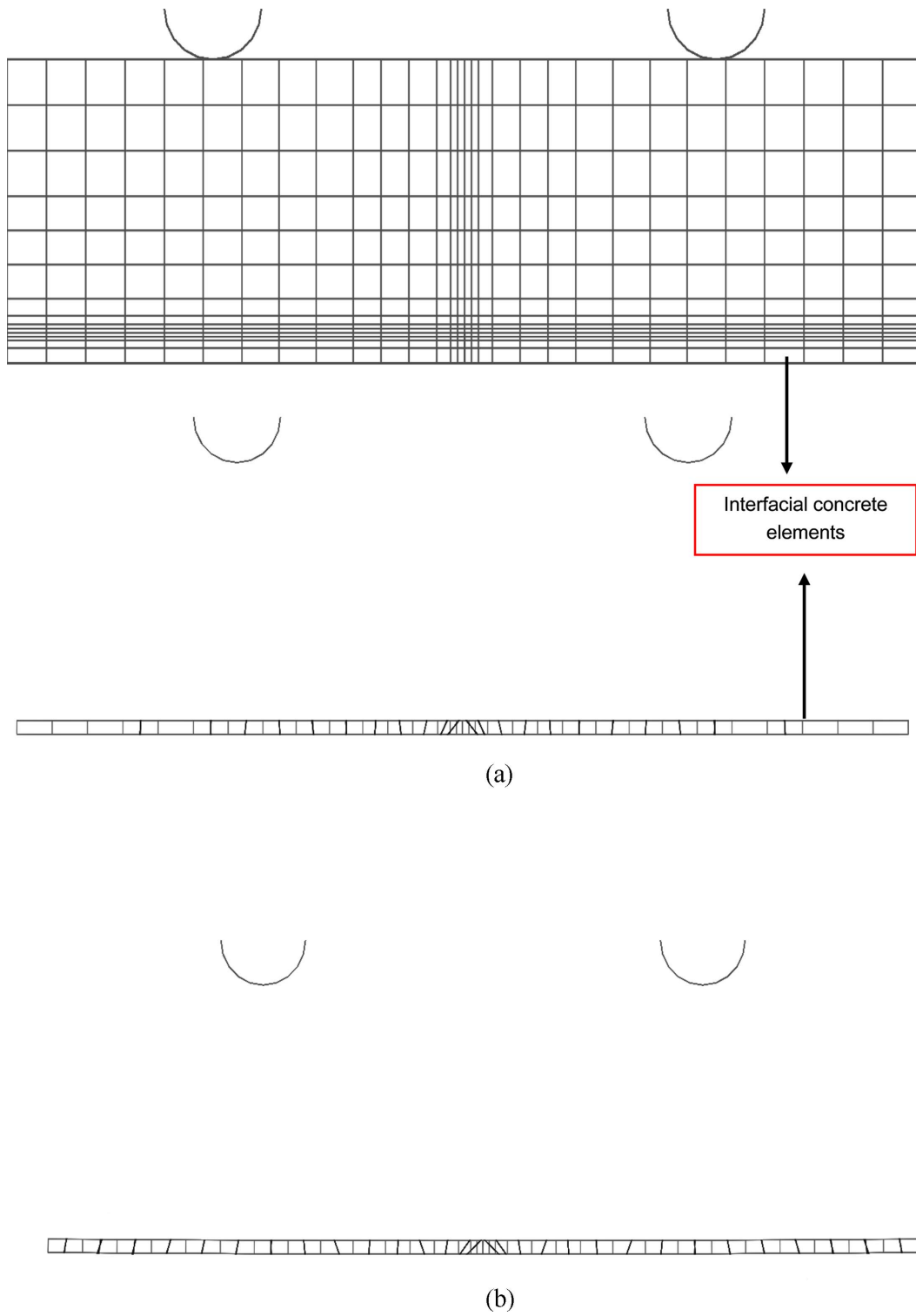
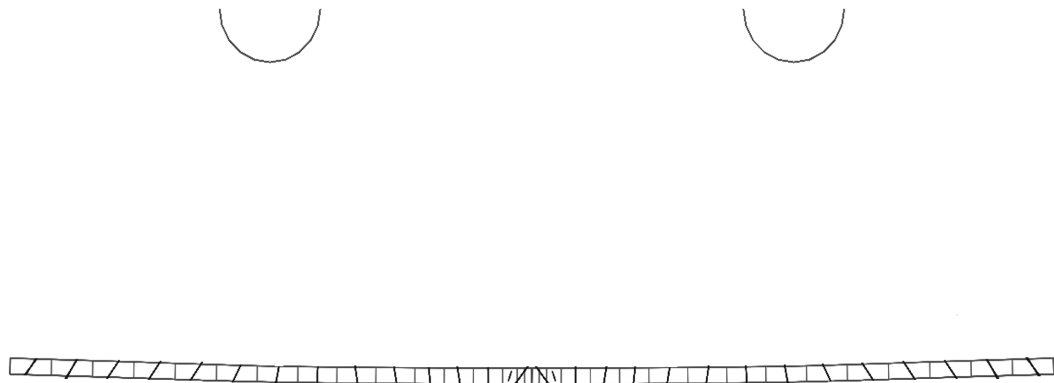


Fig. 28 FE solution of crack evolution in the interfacial concrete elements in CFRP retrofitted RC beam



(c)



(d)

Fig. 28 Continued

the loading progression notch mouth opening increased and cracks at the notch tip propagated. As monotonic loading progressed, cracks distributed along the beam however, major cracks distributed in a space between the two grips. At the final stages of loading, major cracks reached to the top surface of the beam as illustrated in Figs. 27(d) and 27(e). Also, as can be seen in the Fig. 27(e) at the very final steps of loading crack initiated and propagated at the top surface of the beam. The current distribution of cracks implies to the crushing of compressive concrete. It should be noted that prior to the crushing, yielding of tensile steel rebar occurred. Thus, at the failure of these specimens two modes of failure, that were, tensile steel rebar yielding and compressive concrete crushing, developed.

In Fig. 28 FE solution of crack evolution at the interface concrete part between the two grips is illustrated. In the interfacial concrete elements at the vicinity of the CFRP layer, the crack initiation

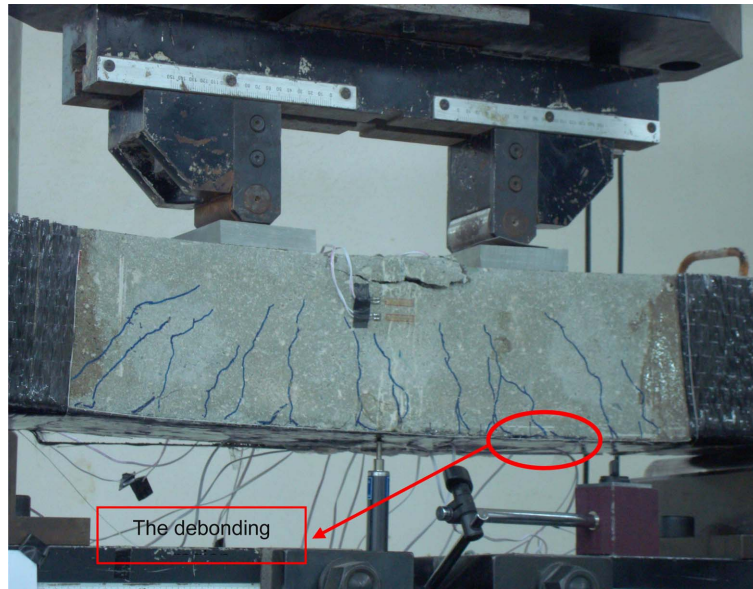


Fig. 29 Failure of tested CFRP retrofitted RC beam and the illustrated debonding region

was almost all over the position between the two grips but mostly at the pre-cracked middle section of the beams and beneath the grips, simultaneously. with the growth of applied load, cracks developed all over the interfacial concrete part and At the same time cracks contours rotated. When angle of cracks contours reached the value of 45° , the interfacial concrete elements commenced to fail and this happened beneath the grips.

Similar event took place in the experimental process. From the Fig. 29, it can be observed that, at the final stages of the loading the interfacial concrete elements outside the region between the two grips and at the vicinity of the grips, were capable of failure. Consequently, at this zone the debonding failure was probable.

Failure modes of failure at the test of the CFRP retrofitted RC beams consisted of crushing of the compressive concrete and rupture of the CFRP and debonding at the interface zone. These modes occurred almost simultaneously at the failure.

5. Conclusions

According to the results presented in the load-deflection diagrams, using the 2 layered CFRP increased the load carrying capacity of about 75% and lessened the ductility. The drop in the diagrams in the CFRP retrofitted beams, was resulted from one or more modes of failure, that were, crushing of the compressive concrete, rupture of the CFRP and debonding of the CFRP from the concrete substrate. In the performed test, the mentioned modes of failure occurred almost simultaneously.

Observing Figs. 18 to 23, it can be noticed that tensile crack spreading in the concrete was so sudden. The drop of the strains in the strain gauges was resulted from the initiation of flexural

cracks at the tensile concrete at the vicinity of the CFRP-concrete, called as, interfacial concrete. At this region and range of the loading, flexural crack began to propagate.

In the present study, the significant parameter in the debonding mode of failure was the tensile concrete separation, which was discussed and illustrated in Figs. 26 to 29. It was calculated and observed that as the tensile cracks in the interfacial concrete elements reached 45° in direction, and stresses in concrete approached the tensile strength, the debonding process happened in the interface at the region outside the grips and at the vicinity of them.

References

- ACI (2008), "Building code requirements for structural concrete and commentary (ACI 318-11)", *American Concrete Institute*, Farmington Hills, MI48331, USA.
- Bizindavyi, L. and Neale, K.W. (1999), "Transfer lengths and bond strengths for composites bonded to concrete", *J. Compos. Constr.*, **3**(4), 153-160.
- Duthinh, D. and Starnes, M. (2004), "Strength and ductility of concrete beams reinforced with CFRP plates and steel", *J. Compos. Constr., ASCE*, **8**(1), 59-69.
- Hu, H.T., Lin, F.M. and Jan, Y.Y. (2004), "Nonlinear finite element analysis of reinforced concrete beams strengthened by fiber-reinforced plastics", *J. Compos. Constr., ASCE*, **63**(3-4), 271-281.
- Huang, J. and Huang, P. (2011), "Three-dimensional numerical simulation and cracking analysis of fiber-reinforced cement-based composites", *Comput. Concrete*, **8**(3), 327-341.
- Goloti, V., Spadea, G. and Swamy, R. N. (2004), "Structural model to predict the failure behavior of plated reinforced concrete beams", *J. Compos. Constr., ASCE*, **8**(2), 104-122.
- Jones, R., Swamy, R.N. and Bouderbalah, A. (1980), "Composite behavior of concrete beams with epoxy bonded external reinforcement", *Int. J. Cement Compos.*, **2**(2), 91-107.
- Kabir, M.Z. and Hojatkashani, A. (2008), "A comparison between finite element and analytical solutions of interfacial stress distribution in a RC beam retrofitted with FRP composite", *Int. J. Sci. Technol. Amirkabir*, **19**, 55-63.
- Labossiere, P., Neale, K.W. and Rochette, P. (2000), "Fiber reinforced polymer strengthening of the Saint-Emelie-de-l'Energie Bridge: design, instrumentation, and field testing", *Can. J. Civil Eng.*, **27**(5), 916-927.
- Lau, K.T., Dutta, P.K., Zhou, L.M. and Hui, D. (2001), "Mechanics of bounds in an FRP bounded concrete beam", *J. Compos., Part B: Eng.*, **32**, 491-502.
- Leung, C.K.Y. (2001), "Delamination failure in concrete beams retrofitted with a bonded plate", *J. Mater. Civil Eng.*, **13**(2), 106-113.
- Macgregor, L.G. (2000), *Modified Hognestad Model for the Compressive Concrete*, Reinforced Concrete Mechanics and Design, Prentice-Hall, NJ.
- Meier, U. (1997), "Post strengthening by continuous fiber laminates in Europe", *Non-metallic(FRP) Reinforcement for Concrete Structures*, Vol. 1, Japan Concrete Institute, 41-56.
- Oehlers, D.J. and Moran, J.P. (1990), "Premature failure of externally plated reinforced concrete beams", *J. Struct. Eng.*, **116**(4), 978-995.
- Owen, D.R.J., Figueiras, J.A. and Damjanic, F. (1983), "Finite element analysis of reinforced and prestressed concrete structures including thermal loading", *Comput. Meth. Appl. Mech. Eng.*, **41**(3), 323-366.
- Quantrill, R.J., Hollaway, L.C. and Thorne, A.M. (1996), "Prediction of the maximum plate and stresses of FRP strengthened beams", *Mag. Concrete Res.*, **48**(177), 343-351.
- Smith, S.T. and Teng, J.G. (2001), "Interfacial stresses in plated beams", *J. Eng. Struct.*, **23**, 857-871.
- Teng, J.G., Chen, J.F., Smith, S.T. and Lam, L. (2002), *FRP-Strengthened RC Structures*, John Wiley & Sons, West Sussex, England.
- Teng, J.G., Lu, X.Z. and Jiang, J.J. (2005), "Bond-slip models for FRP sheet bonded to concrete", *J. Eng. Struct.*, **27**(6), 920-937.
- Triantafyllou, T.C. and Plevris, N. (1992), "Strengthening of RC beams with epoxy bonded fiber composite

- materials”, *Mat. Struct.*, **25**, 201-211.
- Van Gemert, D. (1980), “Repairing of concrete structures by externally bonded steel plates”, *Int. J. Adhesion*, **2**, 67-72.
- Zibara, Y.N., Baluch, M.H. and Sharif, A.M. (1995), “Combined experimental-numerical approach to the characterization of the steel-glue-concrete interface”, *Mat. Struct.*, **28**, 518-525.
- Zou, Y. and Huchelbridge, P.E. (2007), “Simulation of crack growth in FRP reinforced concrete”, *J. Bridge Eng., ASCE*, **12**(2), 237-245.
- Mander, J.B., Priestley, M.J.N. and Park, R. (1988), “Theoretical stress-strain model for confined concrete”, *J. Struct. Eng., ASCE*, **114**(8), 1804-1826.